



Resolution enhancement of wide-field interferometric microscopy by coupled deep autoencoders

ÇAĞATAY IŞIL,¹ MUSTAFA YORULMAZ,¹ BERKAN SOLMAZ,¹ ADIL BURAK TURHAN,² CELALETTİN YURDAKUL,³ SELİM ÜNLÜ,^{3,4} EKMELE OZBAY,^{2,5,6} AND AYKUT KOÇ^{1,*}

¹ASELSAN Research Center, Ankara 06370, Turkey

²NANOTAM-Nanotechnology Research Center, Bilkent University, Ankara 06800, Turkey

³Department of Electrical and Computer Engineering, Boston University, Boston, Massachusetts 02215, USA

⁴Department of Biomedical Engineering, Boston University, Boston, Massachusetts 02215, USA

⁵Department of Electrical Engineering, Bilkent University, Ankara 06800, Turkey

⁶Department of Physics, Bilkent University, Ankara 06800, Turkey

*Corresponding author: aykutkoc@aselsan.com.tr

Received 8 January 2018; revised 26 February 2018; accepted 1 March 2018; posted 2 March 2018 (Doc. ID 319155); published 28 March 2018

Wide-field interferometric microscopy is a highly sensitive, label-free, and low-cost biosensing imaging technique capable of visualizing individual biological nanoparticles such as viral pathogens and exosomes. However, further resolution enhancement is necessary to increase detection and classification accuracy of subdiffraction-limited nanoparticles. In this study, we propose a deep-learning approach, based on coupled deep autoencoders, to improve resolution of images of L-shaped nanostructures. During training, our method utilizes microscope image patches and their corresponding manual truth image patches in order to learn the transformation between them. Following training, the designed network reconstructs denoised and resolution-enhanced image patches for unseen input. © 2018 Optical Society of America

OCIS codes: (180.3170) Interference microscopy; (100.3010) Image reconstruction techniques; (100.6640) Superresolution; (100.4996) Pattern recognition, neural networks.

<https://doi.org/10.1364/AO.57.002545>

1. INTRODUCTION

Microscopy has been important for visualizing biological particles since the invention of the optical microscope in the seventeenth century [1]. Optical microscopy in the visible spectrum has become a ubiquitous and indispensable tool for biological research [2,3]. However, conventional far-field light-scattering microscopy suffers from resolution limitations due to diffraction and visibility contrast for imaging low refractive index biological micro- and nanoparticles. Several techniques, such as fluorescence microscopy [4], interference reflection microscopy [5], and phase contrast microscopy [6], have been proposed for improving contrast [7]. Sensitive wide-field optical detection of nanoparticles has recently been demonstrated using aspheric liquid nanolenses enhancing the contrast [8]. In fluorescence microscopy, the diffraction limit can be surpassed. A variety of techniques have been developed such as stimulated emission depletion microscopy [9], stochastic optical reconstruction microscopy [10], photo-activated localization microscopy [11,12], and spatially structured illumination microscopy (SSIM) [13]. In contrast, conventional

light-scattering microscopy cannot benefit from nonlinearities exploited for resolution enhancement.

Deconvolution is a well-known post-processing technique in microscopy to improve resolution independent of contrast mechanisms. It is achieved by reversing the effects of convolution on a recorded image. This method is beneficial in improving resolution of different kinds of microscope images such as interference images [14], fluorescence images [15], and 3D images [16]. One of the several deconvolution types is the blind deconvolution in which the deconvolution is performed without prior knowledge of the point-spread function [17–20]. There are also other methods such as dictionary-based image reconstruction for resolution enhancement [21].

The interference reflection microscopy takes advantage of interference between the optical scattering signals from the object and a reference reflection that is maximized by adjusting the phase condition to improve the contrast naturally. Despite getting an improvement in contrast, it is still subject to optical deterioration due to the diffraction and background noise. Wide-field interference microscopy is one of the several

techniques of the interference reflection microscopy. In this technique, the signal scattered from nanoparticles interferes with the signal reflected from a specified substrate. The measured interference signal can be maximized by adjusting the optical path difference [22–25]. The common path wide-field interferometric microscopy may be a solution for early diagnosis and prognosis because it is cost-efficient and has a relatively simple setup [23].

Recently, deep-learning-based methods have gained significant attention due to their success in computer vision applications such as visual object classification, object detection, and face recognition [26]. Deep-learning-based models have been effective in extracting the intrinsic (low-dimensional and yet descriptive) information and representations of natural images [27]. Also, these models have started to attract attention in wide-field microscopy [28].

An autoencoder (AE) is a deep-learning-based model that is composed of an encoder and a decoder. The encoder part uses image patches (i.e., small pieces of an image) as input and discovers intrinsic representations of them. Then, in the decoder part, intrinsic representations are used for reconstructing the input image patches [27]. AEs have been employed in many super-resolution methods in image processing because of their success in capturing details in high-resolution images [29–31]. They have also been applied to biotechnological studies [32–34]. Recently, Zeng *et al.* [29] introduced a coupled deep autoencoder (CDA) model, which uses two deep AEs and learns nonlinear mapping between the intrinsic representations of these deep AEs. Low- and high-resolution image patches (LRs and HRs) are provided to obtain the intrinsic representations of image patches by using deep AEs. Then, a nonlinear mapping is estimated between the intrinsic representations by taking advantage of the backpropagation algorithm [35]. After the initialization and nonlinear mapping, LRs pass through the overall network to minimize the mean squared error (MSE) [Eq. (8)] between HRs and network outputs for LRs in a finite number of iterations. The network is optimized by the help of the backpropagation algorithm. This operation is called training of a network. After training, the performance of the network is evaluated by using LRs and HRs, which are previously unseen by the network.

In this study, for the resolution enhancement of the wide-field interferometric microscopy, we propose to use a method based on CDAs. Wide-field microscope images are cropped to obtain image patches with a single L-shaped nanostructure. These small raw image patches (RPs) are taken as LRs in CDA. Then, manual truth image patches (MTPs) are generated artificially by using the corresponding raw image patches and the scanning electron microscope (SEM) images. SEM images of L-shaped nanostructures are given in the Appendix A. MTPs are taken as HRs in CDA. Pairs of RPs and MTPs are used for training. After training, new raw images from interference-enhanced wide-field microscope are passed through the network in order to test the proposed method. By applying the proposed method, the resolution of the wide-field interferometric microscopy is improved, as compared with a reference method that involves standard denoising and blind deconvolution algorithms.

The rest of this paper is organized as follows. Interference-enhanced wide-field microscopy samples containing L-shaped nanostructures and CDAs are presented in Section 2. In Section 3, resolution improvement and denoising performances of the proposed method and the reference method are provided. In Section 4, we summarize the results and conclude with final remarks.

2. RESOLUTION ENHANCEMENT OF WIDE-FIELD INTERFEROMETRIC MICROSCOPY BY COUPLED DEEP AUTOENCODERS

A. Wide-Field Interferometric Microscopy

The wide-field interferometric microscope is a low-cost, easy-to-implement, and yet sensitive device that has a large field of view [24]. This microscope utilizes the interference between the scattered light from the nanoparticles and the reflected light from the layered substrate surface for imaging [22].

The scattered signal (E_s) interferes with the reflected signal (E_r) and propagates through a photodetector. The photodetector measures the interference signal intensity, which is defined as

$$I \propto |E_s + E_r|^2 \propto |E_s|^2 + |E_r|^2 - 2|E_s||E_r|\cos(\theta_{rs}). \quad (1)$$

In Eq. (1), by adjusting the phase difference between E_r and E_s (θ_{rs}), the measured intensity signal can be maximized. In our experiments, an SiO_2 layer, thermally grown on an Si substrate surface, is used. By modulating the thickness of the SiO_2 layer, θ_{rs} can be optimized to ameliorate the interference signal [22].

As a spatially low coherent illumination source, a light emitting diode (LED) is used instead of a coherent light source (a laser), to prevent undesired interferometric fringes in the detector plane [36]. As depicted in Fig. 1(a), we employ a Kohler illumination, where the illumination source is imaged to the back focal plane of the microscope using a 2:1 4-f system with achromatic doublet lenses. Because the LED and back focal plane of the objective are conjugate planes, each point of the light source in the back focal plane produces a plane wave at an incident angle defined by its position in the x - y plane. Thus, this configuration accomplishes a source-free uniform

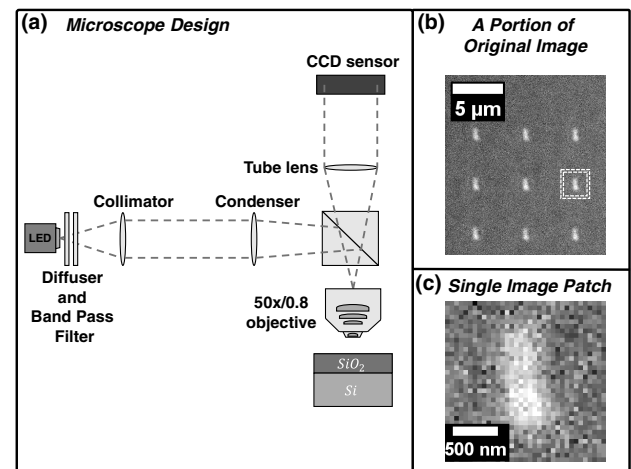


Fig. 1. (a) Schematics of the wide-field interferometric microscope. (b) Image containing 500 nm wide L-shaped SiO_2 nanostructures. (c) Raw image patch containing a single L-shaped nanostructure.

illumination of the object of interest. Therefore, we decided to use an LED source operating at 530 nm. After the illumination, light passes through a diffuser and a bandpass filter. Then, light is directed to a 30 mm lens in order to provide uniform illumination. For a condenser, we use a 60 mm lens. After the condenser, a 50/50 beam splitter is used. Using this configuration, Kohler-type wide-field illumination is accomplished for uniform excitation of the nanoparticles and minimization of the artifacts due to the LED. Then, a 50× microscope objective with NA = 0.8 and a 200 mm tube lens is used to capture the interference images of the nanoparticles on the CCD camera [24].

B. Preparation of Nanoparticle Sample

In order to test the wide-field interferometric microscope, a sample consisting of L-shaped nanostructures are used. The sample contains L-shaped nanostructures that have different sizes; while heights are kept constant at 1000 nm, the widths of the L shapes are varied from 100 nm to 1000 nm.

The sample was imprinted onto a silicon substrate. The first step of the fabrication was the formation of the SiO₂ layer over the sample by a plasma-enhanced vapor deposition coating. A Samco PD-220 NL system was utilized for this process. The coating thickness was 100 nm. Afterward, nanostructures were fabricated by using electron beam lithography (EBL) technology. A Raith eLINE system was used for this fabrication. Hydrogen silsesquioxane (HSQ, XR-1541 from Dow Corning) was chosen as a resist material because it transforms into SiO₂ after electron beam exposure [37]. Therefore, it acted not only as the medium for patterning but also as the material for the desired nanostructures. Another advantage was the reduced writing times, as it was better to use a negative resist for the time efficiency under this process plan. HSQ was diluted to 3% in methyl isobutyl ketone and spin-coated with a spin cycle of 1000 rpm to obtain a thickness of 50 nm. After spin-coating, the sample was baked for 5 min at a temperature of 150°C on a hot plate. HSQ film thickness was confirmed to be 50 nm with the measurements taken in a Filmetrics F20 reflectometer

system. A conductive polymer (aquaSAVE, Mitsubishi Rayon) was spin-coated on top of the HSQ layer to avoid charging.

In the EBL process, we worked with a voltage of 30 kV, with an aperture of 20 mm. The write field area was 100 μm². Exposure dose ranged from 150 μC/cm² to 300 μC/cm² for different exposure patterns. Development was carried out by using a tetramethylammonium hydroxide-based solution (MF-322 from Rohm and Haas) for 35 s, and deionized water was used as a stopper. A Zeiss GeminiSEM 300 SEM was used for the inspection of the fabricated sample (see Section 5 for Appendix A). A sample image captured by the microscope is presented in Fig. 1(b). A single image patch contains a single L-shaped nanostructure, as shown in Fig. 1(c).

C. Coupled Deep Autoencoders for Single Image Super-Resolution

For resolution enhancement of the wide-field interferometric microscope, we used the CDA method on the microscope image patches. The CDA algorithm can be used for various kinds of images. This algorithm has initialization, nonlinear mapping, and final training steps in order to reconstruct resolution-enhanced single images (see Fig. 2). At the initialization stage, LR and HR are used to initialize two distinct deep AEs. The intrinsic representations are formulated by

$$I_b^L = f(W_1 x_i + b_1), \tag{2}$$

$$I_b^H = f(W_3 y_i + b_3). \tag{3}$$

The decoding processes of these two AEs can be described by

$$\hat{y}_i = f(W'_3 I_b^H + b'_3), \tag{4}$$

$$\hat{x}_i = f(W'_1 I_b^L + b'_1), \tag{5}$$

where y_i and x_i are output and input image patch vectors (HRs and LR vectors) in given sets $Y = [y_1, y_2, \dots, y_N]$ and $X = [x_1, x_2, \dots, x_N]$, respectively. Moreover, \hat{y}_i and \hat{x}_i are reconstructed output and input image patch vectors in given

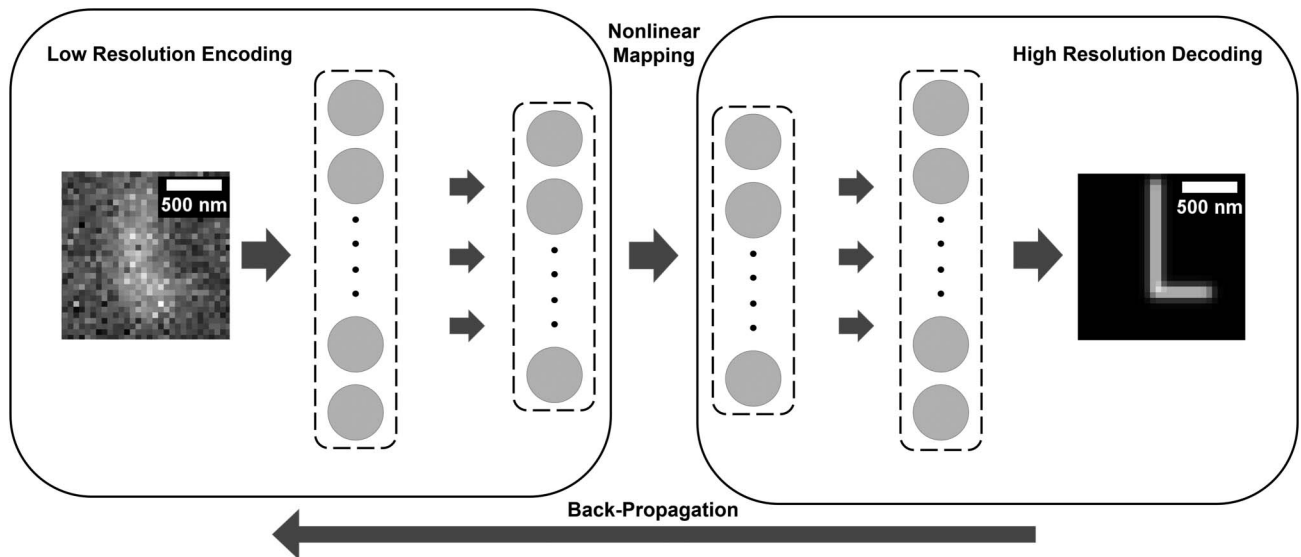


Fig. 2. CDA architecture for resolution enhancement of a raw image patch containing a single L-shaped nanostructure.

sets $\hat{\mathbf{Y}} = [\hat{\mathbf{y}}_1, \hat{\mathbf{y}}_2, \dots, \hat{\mathbf{y}}_N]$ and $\hat{\mathbf{X}} = [\hat{\mathbf{x}}_1, \hat{\mathbf{x}}_2, \dots, \hat{\mathbf{x}}_N]$, respectively. \mathbf{I}_b^L and \mathbf{I}_b^H are intrinsic layer representations of LR and HR, respectively. $(\mathbf{W}_1, \mathbf{W}_3)$ and $(\mathbf{W}'_1, \mathbf{W}'_3)$ denote weight matrices of encoding and decoding networks of AEs, respectively. Also, $(\mathbf{b}_1, \mathbf{b}_3)$ and $(\mathbf{b}'_1, \mathbf{b}'_3)$ represent the bias terms of the encoding and decoding parts of AEs. The function $f(\cdot)$ is the sigmoid activation function and can be obtained by

$$f(t) = \frac{1}{1 + \exp(-t)}. \quad (6)$$

After initialization of deep AEs, intrinsic representations of LR and HRs ($\mathbf{I}_b^L, \mathbf{I}_b^H$) are used to learn the nonlinear mapping between each other by taking advantage of the nonlinear transformation ability of neural networks [26,29]. This mapping can be described by

$$\mathbf{I}_b^H = f(\mathbf{W}'_2 \mathbf{I}_b^L + \mathbf{b}'_2). \quad (7)$$

At the final training step, the complete network is optimized with the help of the backpropagation algorithm [35]. The backpropagation algorithm calculates the gradients of a loss function with respect to the weights of the neural network. It uses the conjugate gradient optimization procedure to reduce the reconstruction error (minimizing the loss) [38]. The conjugate gradient optimization is an iterative method that is used to solve a symmetric, positive definite matrix [39]. As a loss function, the network uses the MSE loss function to improve the network parameters. MSE loss function is calculated as

$$\text{loss} = \sum_i \|\mathbf{y}_i - \hat{\mathbf{y}}_i\|^2. \quad (8)$$

3. RESULTS

For the construction of CDA, we used the dimensionality reduction toolbox [40]. The wide-field interference microscope images are cropped to obtain a data set, consisting of 29-pixel-x-29-pixel-sized RPs of different L-shaped nanostructures, as shown in Fig. 1(c). Furthermore, to enlarge the data set and increase its diversity, RPs are rotated and translated arbitrarily. Moreover, the translated and rotated data set contains synthetic MTPs of corresponding RPs. This data set is separated into three splits: a training split consisting of 80% of the data, a validation split consisting of 10% of the data, and a testing split that contains the rest. 254,000 pairs of RPs and MTPs were used for training the neural network. The testing split contains the remaining 31,000 pairs of RPs and MTPs. After learning the parameters of the network by using the training and validation splits, the test split is used for verifying the enhancement in resolution and image quality.

Convergence criteria for final training was used to stop iterations. MSEs of the previous 100 iterations are averaged for each iteration. When averaged MSEs of the corresponding iteration and the preceding iteration become equivalent, the training is complete. After 1158 iterations, for the generated data set, MSE for the training split and for the validation split converged to 0.0299 and 0.0319, respectively (see Fig. 3).

For the performance evaluation, the proposed method based on the designed CDA network was compared with another technique involving a denoising and blind deconvolution algorithm. A generic moving average filter was used for

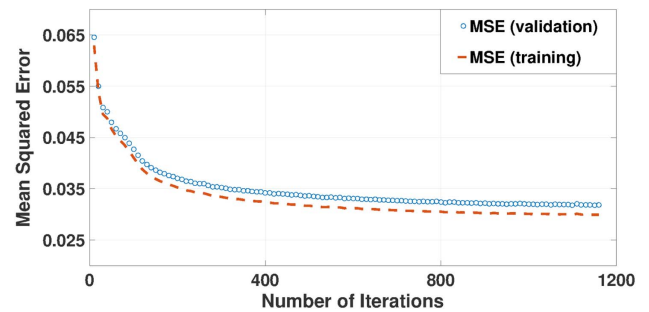


Fig. 3. MSE versus number of iterations.

denoising. As a blind deconvolution method, an iterative blind deconvolution algorithm proposed by Biggs and Andrews was used [41–44].

FWHM values of the output images for both methods were compared in order to demonstrate the improvements in resolution. Then, the SSIM [45] and the peak signal-to-noise ratio (PSNR) of the images were calculated because they allow a quantitative comparison of the denoising and deblurring performances of the proposed method. Moreover, contrast of the images is calculated and compared for both methods.

Five raw images of L-shaped nanostructures with widths varying from 100 to 900 nm were randomly chosen among 31,000 test raw images [see Fig. 4(a)]. The output images of the denoising filter are shown for the raw images in Fig. 4(b). For the reference method, which successively performs denoising and blind deconvolution, we obtain the output images shown in Fig. 4(c). These raw images, which are unseen by the network previously, were passed through the trained network. Then, the corresponding outputs are presented in Fig. 4(d).

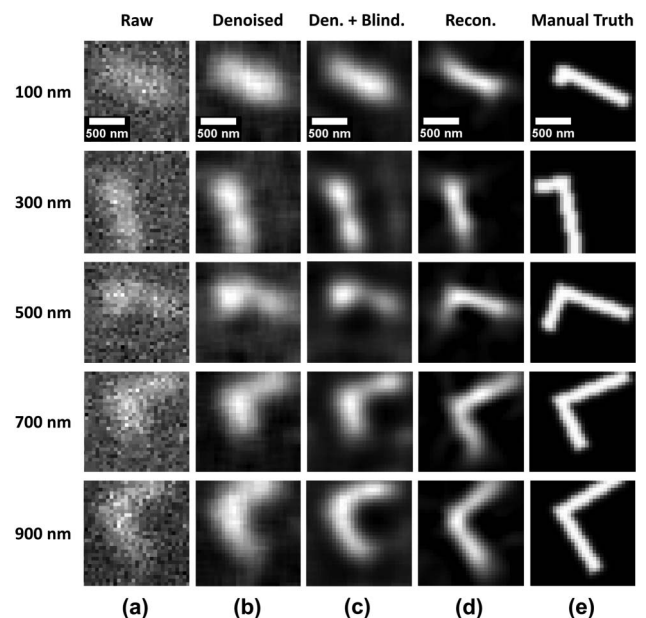


Fig. 4. Images of different methods with widths varying from 100 to 900 nm L-shaped nanostructures. (a) Raw image. (b) Output image of denoising method. (c) Output image of denoising and blind deconvolution method. (d) Reconstructed output image by the proposed method. (e) Manual truth.

We compare the performances of these methods by calculating SSIM and PSNR values by quantifying the similarity of outputs and the manual truth images of L-shaped nanostructures shown in Fig. 4(e). SSIMs and PSNRs of each 31,000 output images of the proposed method and of the reference method are computed by taking the manual truth images as the desired perfect images. Then, average SSIM and PSNR values are calculated. As explained in Table 1, the reconstructed images have a 655% average SSIM improvement with respect to the raw images. Moreover, by using the proposed method, average PSNR is increased by 8.57 db. Results in Table 1 show the denoising and deblurring performance of our method based on a CDA network.

Although the average SSIM and average PSNR results explain the denoising and deblurring performances of the proposed method, for observing the resolution enhancement, the FWHM estimations are also compared. The microscope setup has a FWHM of 404 nm, and the thickness of L-shaped nanostructures was approximately 30 nm. Because the thickness is smaller than the FWHM value of the microscope, horizontal line profiles taken across the heights of the L-shapes from raw images can be considered as a line profile of the point-spread function of the microscope. Therefore, the line profiles of the output L-shaped images for each method were used to estimate the approximate new FWHM values after applying the methods.

In Fig. 5, the line profiles and Gaussian fitted curves from the output images of different methods are shown. In Fig. 5 from (a) to (d), the resolution improvement of different methods can be observed. For comparison, the line profile of the manual truth image is shown in Fig. 5(e). Due to the quantization and alignment errors in the manual truth data set generation, we can observe a shift in the line profile of the manual truth [Fig. 5(e)] with respect to the true position of the nanoparticles. The quantization and alignment errors are different and small for each element in the data set, but the proposed method neutralizes these errors and gives more accurate line profiles [Fig. 5(d)]. In Table 2, we have the best resolution enhancement performance for our methods based on the CDA network. While the resolutions of raw images were improved by the denoising and blind deconvolution-based method by 25%, our method, based on the CDA network, gives an improvement of 44.5%. Raw images of L-shaped nanostructures had FWHM values of 487 nm. The FWHM values of the raw images were different than the microscope FWHM value because the LED source, used for the excitation, has a broad bandwidth and lower beam quality than the monochromatic laser sources.

Moreover, by using 11,000 test images, average contrasts of the output images of the methods are tabulated in Table 3. We

Table 1. SSIM and PSNR Performance of the Proposed and the Reference Method on 31,000 Test Images

Image Patches	Average SSIM	Average PSNR (db)
Raw	0.0528	8.5365
Denoised	0.0913	10.6071
Denoised + Deconvolved	0.1186	12.2942
Reconstruction (proposed)	0.3988	17.1017

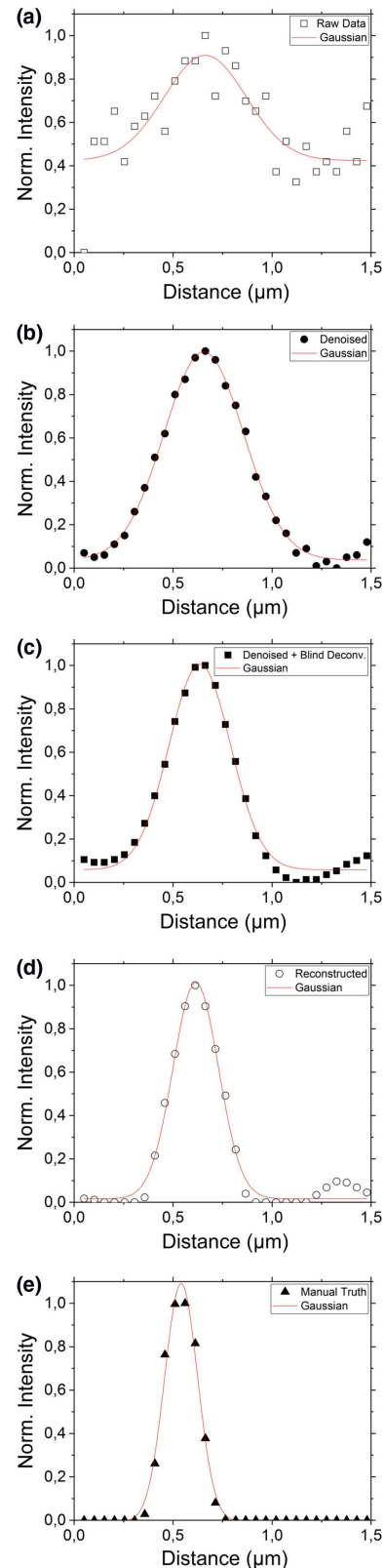


Fig. 5. Line profiles and Gaussian fitted curves from output images of different techniques. (a) Raw image. (b) Output image of denoising. (c) Output image of denoising and blind deconvolution method. (d) Reconstructed image by the proposed method. (e) Manual truth.

Table 2. FWHM Values of the Output Images of a 700 nm Wide L-Shaped Nanostructure for Several Methods

Images	FWHM (nm)
Raw	487.34
Denoised	474.81
Denoised + Deconvolved	366.75
Reconstruction (proposed)	270.51

Table 3. Contrast Improvement of the Proposed and Reference Methods on 11,000 Test Images

Images	Avg. Contrast
Raw	0.31
Denoised	0.19
Denoised + Deconvolved	0.39
Reconstruction (proposed)	65.29

calculated the contrast in two steps. First, the background mean of the image is subtracted from the peak image value. Then, the difference is normalized by the background mean. In Table 3, the reconstructed images have the highest contrast values. Note that the contrast of the manual truth images is infinite because the intensity level of the background is zero. That means the proposed method improves not only the resolution and the PSNR but also the contrast of the wide-field interferometric microscope images.

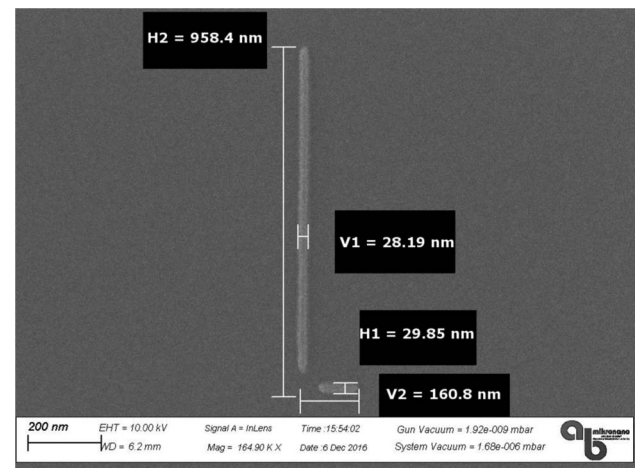
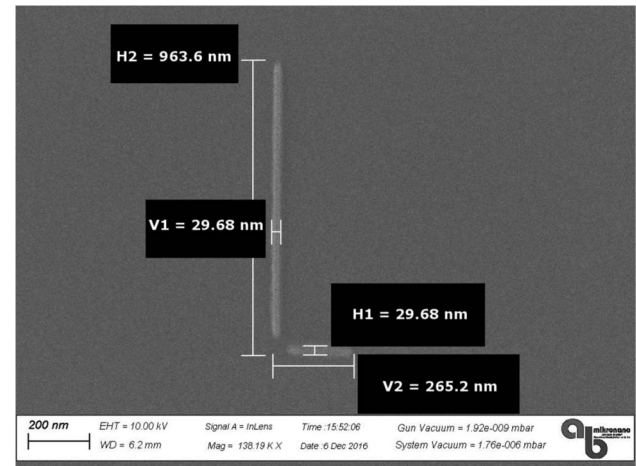
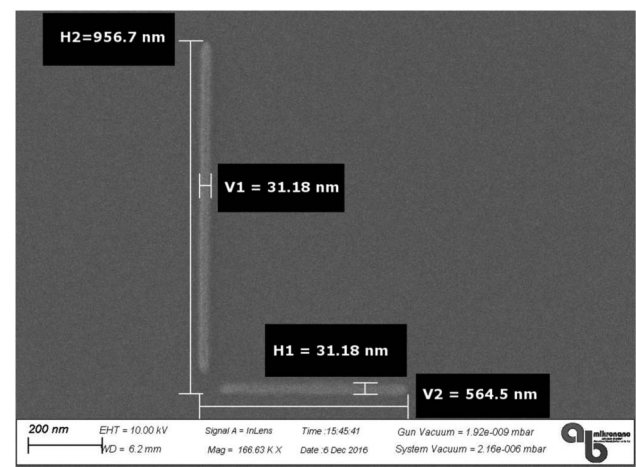
4. CONCLUSION

This study demonstrated the resolution enhancement of the interferometric wide-field microscopy with the CDA network. The CDA network was trained with raw and manual truth image patches. Then, the performance of the network was evaluated by using raw images that are not present in the training set. The reconstructed image patches and the outputs of other methods are given in Fig. 4. The proposed method was compared with a reference method involving denoising and blind deconvolution algorithms. In terms of deblurring and denoising performance, the proposed method reports the highest average SSIM and average PSNR values. In terms of the resolution enhancement, the performance of the proposed method, as measured by FWHM values, is also shown to be superior. Therefore, we can state that the proposed method outperforms the other methods.

To conclude, our novel approach utilizing wide-field interferometric microscopy and CDA is advantageous for biotechnology applications because it can be used for not only the wide-field interferometric microscope but also for other types of microscopes. Moreover, the method can provide faster, cheaper, and more accurate early diagnosis and prognosis with its sensitive and high-resolution measurement capabilities.

APPENDIX A

SEM images of different L-shaped nanostructures are shown in Figs. 6–9. Please note that the widths of the nanoparticles from the SEM images are lower than the desired widths mentioned

**Fig. 6.** SEM image of 200 nm width L-shaped nanostructures.**Fig. 7.** SEM image of 300 nm width L-shaped nanostructures.**Fig. 8.** SEM image of 600 nm width L-shaped nanostructures.

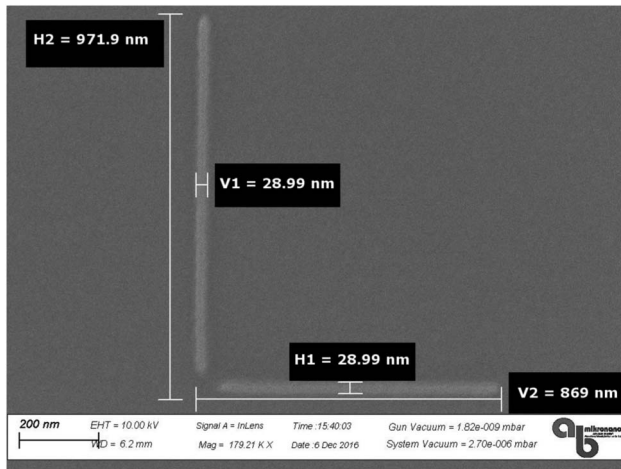


Fig. 9. SEM image of 800 nm width L-shaped nanostructures.

in the captions of the figures due to the imperfections in preparation of the nanoparticle sample. The desired widths are assumed to be 100, 200, 300, 400, 500, 600, 700, 800, 900, and 1000 nm. We map the intermediate values to the closest quantized widths we desired. This assumption is important for MTP generation because 1 pixel corresponds to 51 nm in RPs, and the size of RPs is 29 pixels \times 29 pixels.

Funding. Türkiye Bilimler Akademisi (TÜBA); TUBITAK, BIDEB 2232 (1109B321600054, 1109B321600248).

Acknowledgment. One of the authors (E.O.) acknowledges partial support from the Turkish Academy of Sciences. M. Y. and B. S. acknowledges the support from TUBITAK, BIDEB 2232.

REFERENCES

- N. Lane, "The unseen world: reflections on Leeuwenhoek (1677) 'concerning little animals'," *Philos. Trans. R. Soc. B* **370**, 20140344 (2015).
- F. Kulzer and M. Orrit, "Single molecule optics," *Annu. Rev. Phys. Chem.* **55**, 585–611 (2004).
- J. Olson, S. Dominguez-Medina, A. Hoggard, L.-Y. Wang, W.-S. Chang, and S. Link, "Optical characterization of single plasmonic nanoparticles," *Chem. Soc. Rev.* **44**, 40–57 (2015).
- M. R. Young, "Principles and technique of fluorescence microscopy," *J. Cell Sci.* **s3**-102, 419–449 (1961).
- A. Curtis, "The mechanism of adhesion of cells to glass," *J. Cell Biol.* **20**, 199–215 (1964).
- F. Zernike, "How I discovered phase contrast," *Science* **121**, 345–349 (1955).
- M. Mir, S. D. Babacan, M. Bednarz, M. N. Do, I. Golding, and G. Popescu, "Visualizing escherichia coli sub-cellular structure using sparse deconvolution spatial light interference tomography," *PLoS ONE* **7**, e39816 (2012).
- O. Mudanyali, E. McLeod, W. Luo, A. Greenbaum, A. F. Coskun, Y. Hennequin, C. P. Allier, and A. Ozcan, "Wide-field optical detection of nanoparticles using on-chip microscopy and self-assembled nanolenses," *Nat. Photonics* **7**, 247–254 (2013).
- S. W. Hell and J. Wichmann, "Breaking the diffraction resolution limit by stimulated emission: Stimulated-emission-depletion fluorescence microscopy," *Opt. Lett.* **19**, 780–782 (1994).
- M. J. Rust, M. Bates, and X. Zhuang, "Sub-diffraction-limit imaging by stochastic optical reconstruction microscopy (storm)," *Nat. Methods* **3**, 793–796 (2006).
- E. Betzig, G. H. Patterson, R. Sougrat, O. W. Lindwasser, S. Olenych, J. S. Bonifacino, M. W. Davidson, J. Lippincott-Schwartz, and H. F. Hess, "Imaging intracellular fluorescent proteins at nanometer resolution," *Science* **313**, 1642–1645 (2006).
- S. T. Hess, T. P. Girirajan, and M. D. Mason, "Ultra-high-resolution imaging by fluorescence photoactivation localization microscopy," *Biophys. J.* **91**, 4258–4272 (2006).
- M. G. Gustafsson, "Nonlinear structured-illumination microscopy: wide-field fluorescence imaging with theoretically unlimited resolution," *Proc. Natl. Acad. Sci. USA* **102**, 13081–13086 (2005).
- S. D. Babacan, Z. Wang, M. Do, and G. Popescu, "Cell imaging beyond the diffraction limit using sparse deconvolution spatial light interference microscopy," *Biomed. Opt. Express* **2**, 1815–1827 (2011).
- P. Sarder and A. Nehorai, "Deconvolution methods for 3-D fluorescence microscopy images," *IEEE Signal Process. Mag.* **23**(3), 32–45 (2006).
- J. G. McNally, T. Karpova, J. Cooper, and J. A. Conchello, "Three-dimensional imaging by deconvolution microscopy," *Methods* **19**, 373–385 (1999).
- A. S. Carasso, D. S. Bright, and A. E. Vladar, "Apex method and real-time blind deconvolution of scanning electron microscope imagery," *Opt. Eng.* **41**, 2499–2514 (2002).
- G. Ayers and J. C. Dainty, "Iterative blind deconvolution method and its applications," *Opt. Lett.* **13**, 547–549 (1988).
- M. Keuper, T. Schmidt, M. Temerinac-Ott, J. Padeken, P. Heun, O. Ronneberger, and T. Brox, "Blind deconvolution of widefield fluorescence microscopic data by regularization of the optical transfer function (OTF)," in *Proceedings of the IEEE Conference on Computer Vision and Pattern Recognition (CVPR)* (2013), pp. 2179–2186.
- W. E. Vanderlinde and J. N. Caron, "Blind deconvolution of SEM images," in *International Symposium for Testing and Failure Analysis* (2007), vol. **33**, p. 97.
- T. B. Cilingiroglu, A. Uyar, A. Tuysuzoglu, W. C. Karl, J. Konrad, B. B. Goldberg, and M. S. Ünlü, "Dictionary-based image reconstruction for superresolution in integrated circuit imaging," *Opt. Express* **23**, 15072–15087 (2015).
- O. Avci, R. Adato, A. Y. Ozkumur, and M. S. Ünlü, "Physical modeling of interference enhanced imaging and characterization of single nanoparticles," *Opt. Express* **24**, 6094–6114 (2016).
- O. Avci, N. L. Ünlü, A. Y. Özkuur, and M. S. Ünlü, "Interferometric reflectance imaging sensor (IRIS) a platform technology for multiplexed diagnostics and digital detection," *Sensors* **15**, 17649–17665 (2015).
- M. Yorulmaz, C. Isil, E. Seymour, C. Yurdakul, B. Solmaz, A. Koc, and M. S. Ünlü, "Single-particle imaging for biosensor applications," *Proc. SPIE* **10438**, 104380I (2017).
- O. Avci, C. Yurdakul, and M. S. Ünlü, "Nanoparticle classification in wide-field interferometric microscopy by supervised learning from model," *Appl. Opt.* **56**, 4238–4242 (2017).
- Y. LeCun, Y. Bengio, and G. Hinton, "Deep learning," *Nature* **521**, 436–444 (2015).
- G. E. Hinton and R. R. Salakhutdinov, "Reducing the dimensionality of data with neural networks," *Science* **313**, 504–507 (2006).
- Y. Rivenson, Z. Göröcs, H. Günaydin, Y. Zhang, H. Wang, and A. Ozcan, "Deep learning microscopy," *Optica* **4**, 1437–1443 (2017).
- K. Zeng, J. Yu, R. Wang, C. Li, and D. Tao, "Coupled deep autoencoder for single image super-resolution," *IEEE Trans. Cybern.* **47**, 27–37 (2017).
- Z. Cui, H. Chang, S. Shan, B. Zhong, and X. Chen, "Deep network cascade for image super-resolution," in *European Conference on Computer Vision* (Springer, 2014), pp. 49–64.
- T. Guo, H. S. Mousavi, and V. Monga, "Deep learning based image super-resolution with coupled backpropagation," in *IEEE Global Conference on Signal and Information Processing (GlobalSIP)* (IEEE, 2016), pp. 237–241.
- A. Gogna, A. Majumdar, and R. K. Ward, "Semi-supervised stacked label consistent autoencoder for reconstruction and analysis

- of biomedical signals," *IEEE Trans. Biomed. Eng.* **64**, 2196–2205 (2017).
33. Y. Lai, F. Chen, S. Wang, X. Lu, Y. Tsao, and C. Lee, "A deep denoising autoencoder approach to improving the intelligibility of vocoded speech in cochlear implant simulation," *IEEE Trans. Biomed. Eng.* **64**, 1568–1578 (2017).
34. J. Xu, L. Xiang, Q. Liu, H. Gilmore, J. Wu, J. Tang, and A. Madabhushi, "Stacked sparse autoencoder (SSAE) for nuclei detection on breast cancer histopathology images," *IEEE Trans. Med. Imaging* **35**, 119–130 (2016).
35. D. E. Rumelhart, G. E. Hinton, and R. J. Williams, "Learning representations by back-propagating errors," *Nature* **323**, 533–536 (1986).
36. T. I. Karu, "Light Coherence," (2011), <http://photobiology.info/Coherence.html>.
37. R. Evans, P. Douglas, and H. Burrow, *Applied Photochemistry* (Springer, 2014).
38. M. R. Hestenes and E. Stiefel, "Methods of conjugate gradients for solving linear systems," *J. Res. Nat. Bur. Stand.* **49**, 409–436 (1952).
39. K. Atkinson, *Numerical Solution of Systems of Linear Equations* (Wiley, 1978).
40. L. van der Maaten, "MATLAB Toolbox for Dimensionality Reduction," (2017), <https://lvdmaaten.github.io/drtoolbox>.
41. A. V. Oppenheim and R. Schaffer, *Digital Signal Processing*, MIT Video Course (Prentice-Hall, 1975).
42. T. J. Holmes, S. Bhattacharyya, J. A. Cooper, D. Hanzel, V. Krishnamurthi, W.-C. Lin, B. Roysam, D. H. Szarowski, and J. N. Turner, *Light Microscopic Images Reconstructed by Maximum Likelihood Deconvolution* (Springer, 1995), pp. 389–402.
43. E. Y. Lam and J. W. Goodman, "Iterative statistical approach to blind image deconvolution," *J. Opt. Soc. Am. A* **17**, 1177–1184 (2000).
44. R. J. Hanisch, R. L. White, and R. L. Gilliland, *Deconvolution of Hubble Telescope Images and Spectra* (Academic, 1997), pp. 310–360.
45. Z. Wang, A. C. Bovik, H. R. Sheikh, and E. P. Simoncelli, "Image quality assessment: from error visibility to structural similarity," *IEEE Trans. Image Process.* **13**, 600–612 (2004).